Chapter 4
Laboratory Investigations on the Hydraulic Fracturing of Granite Cores

Li Zhuang, Sunggyu Jung, Melvin Diaz, and Kwang Yeom Kim

Abstract This chapter introduces laboratory studies on the hydraulic fracturing of granite cores. Some of the most important factors influencing fracturing are considered, including injection rate, fluid infiltration, fluid viscosity, borehole size, and injection scheme. Results from acoustic emission monitoring help elucidate the fracturing process. Hydraulic fractures of granite samples are observed and analysed at the mineral scale with the aid of X-ray scanning and Computed Tomography. A first attempt to investigate the initiation and propagation of hydraulic fractures in granite drill cores during cyclic injection is presented.

Keywords Granite · Hydraulic fracturing · AE monitoring · Fracture propagation · Fluid infiltration · Fluid viscosity · X-ray CT

4.1 Introduction

Hydraulic fracturing is widely used for in situ stress measurement and reservoir engineering. Recent developments of enhanced geothermal systems have brought attention to hydraulic fracturing in hot dry rock. Unlike the sedimentary rock formations found in traditional oil and gas reservoirs, geothermal reservoirs usually occur within crystalline rocks such as granite and gneiss. HDR often has low or near-

L. Zhuang
Korea Institute of Civil Engineering and Building Technology, Goyang, Republic of Korea
e-mail: zhuangli@kict.re.kr

S. Jung · M. Diaz
Korea University of Science and Technology, Daejeon, Republic of Korea
e-mail: fortheothers@kict.re.kr; mdiaz@kict.re.kr

K. Y. Kim (✉)
Korea Institute of Civil Engineering and Building Technology, Goyang, Republic of Korea

Korea University of Science and Technology, Daejeon, Republic of Korea
e-mail: yeommykim@gmail.com

B. Shen et al. (eds.), *Modelling Rock Fracturing Processes*,
https://doi.org/10.1007/978-3-030-35525-8_4

zero permeability, which has to be enhanced by hydraulic stimulation to make the reservoir more permeable and hence accessible. There are two main methods of hydraulic stimulation, hydro-fracturing and hydro-shearing, and the choice between them strongly depends on the geological formation and rock stress conditions (Gischig and Preisig 2015). Hydro-fracturing creates new tensile fractures in the rock mass, while hydro-shearing initiates slip at pre-existing fractures and faults. Regardless of the stimulation method, induced seismicity due to fluid injection must be considered (Zang et al. 2019). The injection scheme can be optimized to enhance permeability while controlling the induced seismicity.

Many experimental studies have investigated the hydraulic fracturing behaviour of rocks, including sandstone, shale, granite, and artificial rock. The hydraulic fracturing behaviours of different granites have been reported by Haimson (1975, 1999), Haimson and Lee (1980), Solberg et al. (1980), Haimson and Doe (1983), Haimson and Zhao (1991), Zhao et al. (1996), Ishida et al. (1997, 2000, 2004, 2012), Chen et al. (2015), Zhuang et al. (2019a, b) and Stephansson et al. (2019). Various theoretical models have been presented to predict the breakdown pressure (BP) during hydraulic fracturing, but none of these perform well in explaining the observed breakdown phenomena (Guo et al. 1993). Hydraulic fracturing is a complex process, and the initiation and propagation of fractures in different types of rocks have not been fully elucidated.

To understand further the hydraulic fracturing behaviour of granites, a series of tests was performed on granite core samples, and the results were analysed with a focus on the influences of injection rate, fluid infiltration, fluid viscosity, borehole size, and injection scheme. In particular, acoustic emission (AE) monitoring and X-ray computed tomography (CT) scanning were employed to investigate the initiation and propagation of hydraulic fracturing and to characterize the fractures.

4.2 Experimental Setup

4.2.1 Hydraulic Fracturing Test Equipment

Figure 4.1 shows the equipment used for hydraulic fracturing tests on core samples. Vertical pressure, confining pressure, and injection pressure are supplied by hydraulic pumps. Fluid is injected from the bottom of the rock sample, and rubber O-rings are installed between the sample and the loading plates to prevent leakage of the injected fluid from the top and bottom of the sample. Recorded data include the displacement of the injection piston (for calculating injection volume), the injection pressure and the vertical and confining pressures.

Figure 4.2 shows photographs of the main apparatus, including the monitoring and recording unit, the hydraulic pump, and the hydraulic fracturing equipment with triaxial cells mounted on the workbench of the X-ray chamber. The cells are either

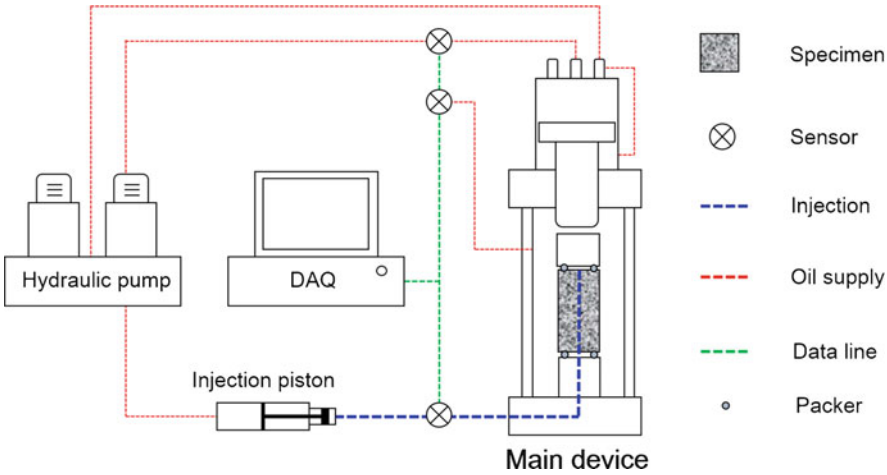

Fig. 4.1 Schematic diagram of the hydraulic fracturing test system

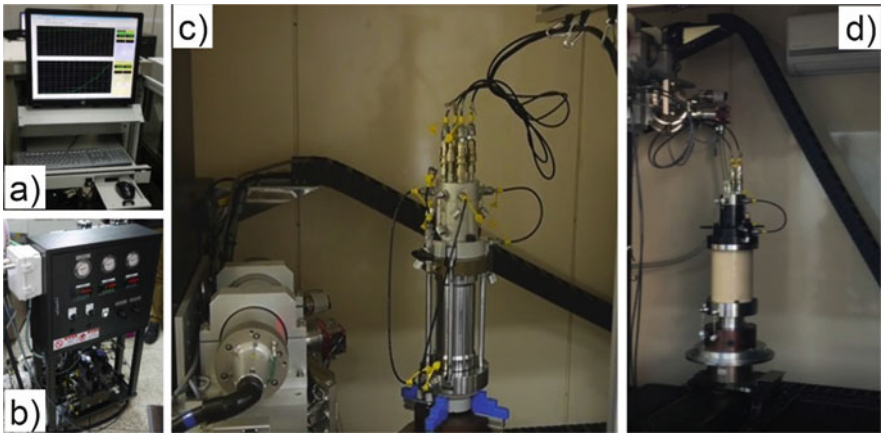

Fig. 4.2 Hydraulic fracturing test equipment: (**a**) monitoring and record unit, (**b**) hydraulic pump, (**c**) steel triaxial cell and (**d**) PEEK triaxial cell combining with CT scanning

made in steel or polyether ether ketone (PEEK). The maximum confining and injection pressures for the system are 20 MPa and 35 MPa, respectively.

Figure 4.3 shows the sequence for setting up the core sample. The sample rests on a pedestal, and injection fluid is supplied from the bottom. Circular plates with O-rings prevent fluid leakage. Later, a thermo-responsive plastic membrane is used to cover the sample, and additional O-rings are placed. The upper part of the equipment, which is responsible for applying vertical load, is suspended by four steel bars. There is a rotation connection at the bottom of the lower platen, which allows the whole loading system to be installed on the rotating table in the X-ray

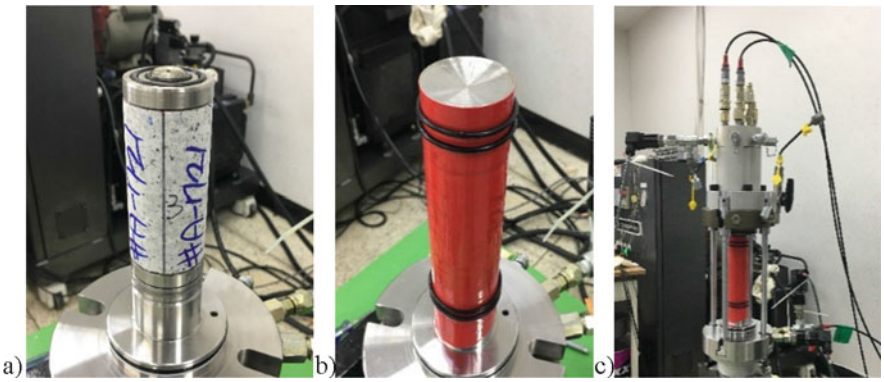

Fig. 4.3 Experimental preparation under zero confining pressure: (**a**) sample setting, (**b**) membrane and O-ring installation, (**c**) vertical loading platen setting

Fig. 4.4 Granite quarry in Pocheon area, South Korea

chamber. The whole testing system can rotate up to 720°, allowing the sample to be scanned during testing.

4.2.2 Test Samples

The test samples are Pocheon granite, obtained from a quarry in Pocheon, South Korea (Fig. 4.4). X-ray diffraction analysis shows its main components to be plagioclase (35.9%), quartz (35.7%), microcline (25.8%) and biotite (2.6%). The average measured effective porosity is 0.66%. This granite shows mild but clear anisotropy, with three typical cleavages of rift (R), grain (G) and hardway (H), which have different densities of microcracks (Zhuang et al. 2016a). As shown in Fig. 4.5, the samples are classified by the coring direction: the R, G and H labels refer to specimens cored perpendicular to those cleavage planes. Table 4.1 lists the basic physical and mechanical properties of the granite, considering the anisotropy.

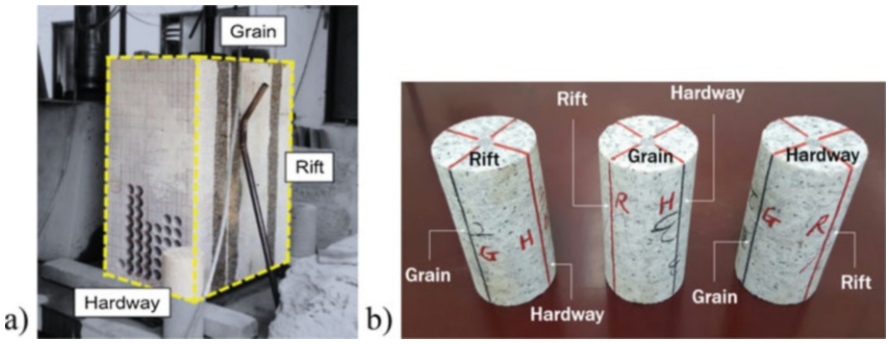

Fig. 4.5 Granite samples: (**a**) coring from a granite block, (**b**) Core samples with different relative positions of cleavages

Table 4.1 Main physical and mechanical properties of Pocheon granite

Specimen /Plane	Hydraulic conductivity[a] (m/s)	Elastic modulus[b] (GPa)	BTS[c] (MPa)	UCS[b] (MPa)	Fracture toughness[b] ($MPa.m^{0.5}$)
Rift (R)	1.09E-10	57.53	6.05	220.01	0.963
Grain (G)	8.34E-11	55.09	8.20	194.62	1.211
Hardway (H)	7.20E-11	58.47	8.83	192.10	1.583

Zhuang et al. (2019a)
[a]Average of three test values
[b]Average of five test values
[c]Average of 20 test values. Hydraulic conductivity, Brazilian tensile strength (BTS) and tensile fracture toughness were measured along the rift, grain and hardway planes. Elastic modulus and uniaxial compressive strength (UCS) were measured on the R, G and H specimens

4.3 Testing Conditions

4.3.1 Stress Conditions

The external stresses applied to a sample directly influence its breakdown pressure and fracture propagation. The first breakdown pressure model by Hubbert and Willis (1957) is

$$P_b = 3\sigma_{Hmin} - \sigma_{Hmax} + \sigma_T - P_0 \tag{4.1}$$

where σ_{Hmax} and σ_{Hmin} are the major and minor horizontal principle stresses, respectively, σ_{T} is the hydraulic tensile strength, and P_0 is the initial pore pressure.

When the vertical stress is the maximum principal stress, the tensile induced hydraulic fractures are vertical, parallel to the maximum horizontal principal stress. Biaxial hydraulic fracturing tests on cylindrical samples employ equal major and minor horizontal principle stresses, which are equal to the confining pressure σ_p. Therefore, Eq. (4.1) becomes

$$\boldsymbol{P_b = 2\sigma_p + \sigma_T - P_0} \tag{4.2}$$

However, poroelastic effects cause experimental breakdown pressures to follow a linear relationship with confining pressure, meaning the coefficient is ~1.0 instead of the theoretical value of 2.0. This phenomenon has also been reported elsewhere for both granite (Rummel 1987) and other types of rock, including sandstone and marble (Brenne et al. 2013). Haimson and Fairhurst (1967) proposed a breakdown pressure model considering the poroelastic effect, which for biaxial test conditions can be expressed as

$$P_b = \frac{2\sigma_p + \sigma_T}{2 - \alpha\left(\frac{1-2\upsilon}{1-\upsilon}\right)} - P_0 \tag{4.3}$$

where α is Biot's poroelstic parameter and υ is Poisson's ratio.

4.3.2 Injection Fluid and Injection Control

Laboratory hydraulic fracturing experiments can employ a variety of fluids (e.g., water, oil and gases), although water is often used. The viscosity of the injected fluid has a strong influence on the fracturing results (Ishida et al. 2004; Chen et al. 2015), and this will be discussed in the next section.

In the laboratory, fluid can be injected by controlling the injection rate or the pressurization rate (Detournay and Cheng 1992). In the field, stimulation is usually controlled by the flow rate. The terms injection rate, flow rate and pumping rate often appear in the literature to represent the amount of fluid injected into a borehole in a certain time.

4.3.3 Hydraulic Fracturing and Sleeve Fracturing

For special tests such as sleeve fracturing, the borehole is covered by a membrane or rubber tube to prevent injection fluid from infiltrating the rock sample, meaning that the poroelastic effect due to fluid infiltration can be ignored.

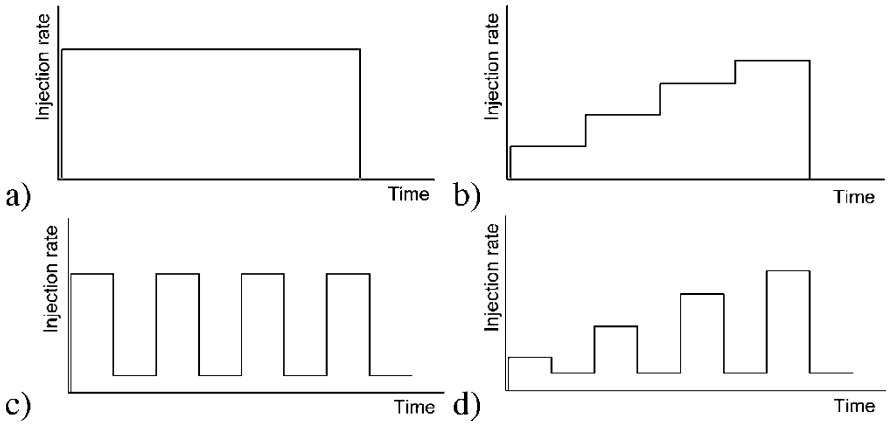

Fig. 4.6 Different schemes of injection rate (vertical axis) – time (horizontal axis): (**a**) Constant rate monotonic injection, (**b**) Stepwise rate monotonic injection, (**c**) Cyclic injection and (**d**) Cyclic progressive injection

4.3.4 Continuous Injection and Cyclic Injection

Conventional hydraulic fracturing usually involves continuous fluid injection until hydraulic breakdown. A massive injection without controlling the injection rate or volume could induce significant seismicity with negative environment effects. Cyclic hydraulic fracturing was proposed by Zang et al. (2013) in an effort to reduce the induced seismicity. It involves alternating between high and low (or zero) injection rates instead of continuous injection, and the injection pressure is lowered frequently to allow stress relaxation at the fracture tip. Figure 4.6 compares two continuous and two cyclic injection schemes, where injection rate varies with the injection time. Recent works have proved the concept and quantitatively evaluated various injection schemes at different scales (Zhuang et al. 2016b, 2017, 2018a, b, 2019b; Zang et al. 2017, 2019; Diaz et al. 2018a, b; Hofmann et al. 2018a, b; Zimmermann et al. 2019).

4.4 Experimental Results

4.4.1 Influence of Confining Pressure

Figure 4.7 shows the relationship between BP and confining pressure for R specimens at an injection rate of 25 mm^3/s and for H specimens at an injection rate of 100 mm^3/s. The specimens have borehole diameter of 8 mm. In both cases, BP increases linearly with increasing confining pressure. Linear fitting yields a ratio

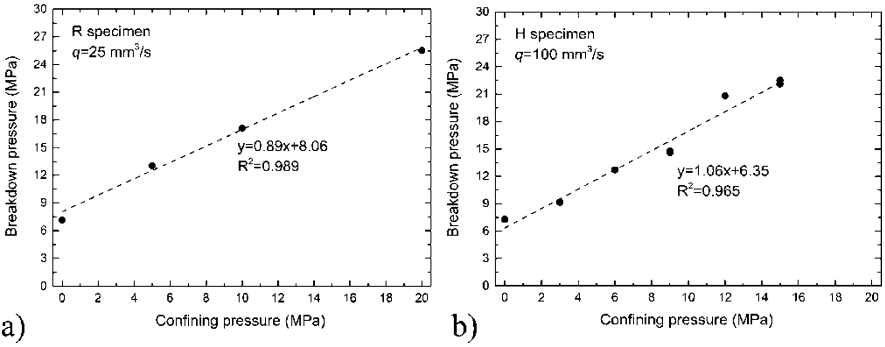

Fig. 4.7 Relationship between breakdown pressure and confining pressure: (**a**) R specimen at $q = 25$ mm^3/s, (**b**) H specimen at $q = 100$ mm^3/s

between them of 0.89 for R specimens and 1.06 for H specimens. The smaller value for the R specimens is due to the lower injection rate.

Previous studies have shown that BP is usually higher at a higher injection rate (Zhuang et al. 2019a). According to the first breakdown model suggested by Hubbert and Willis (1957), if the rock is impermeable, the ratio of BP to confining pressure should be 2.0. However, even for low-permeability granite, water infiltrates the specimen in laboratory tests, leading to a non-negligible poroelastic effect. The model of Haimson and Failhurst (1967) in Eq. (4.3) and extensions of this model including Biot's poroelastic parameter can be used to explain the result. Biot's poroelastic parameter varies among rock types.

4.4.2 Borehole Size Effect

Haimson and Zhao (1991) reported that breakdown pressures measured in laboratory tests are essentially unaffected by the borehole diameter if it is at least 20 mm; the results are thus directly applicable to the interpretation of field data. However, experimental results by Morita et al. (1996) show a clear decrease in the breakdown pressure of Berea sandstone when the borehole size increased from 38 to 100 mm.

Figure 4.8 shows granite samples (all 50 mm diameter, D, and 100 mm height) with cylindrical cross-sections parallel to the grain or hardway plane (i.e., G or H samples). The borehole diameters, d, are 5, 8, 12 and 16 mm, giving d/D ratios of 1:10, 1:6.3, 1:4.2 and 1:3.6, respectively. The influence of the d/D ratio was investigated using water injected at two different rates (50 and 100 mm^3/s).

Figure 4.9 compares the induced fractures surrounding the borehole. The X-ray CT images have a resolution of 0.0317 mm/pixel and show only the area near the borehole instead of the full section of the specimen. The fractures are generated mainly along the rift plane, which has the weakest tensile strength. Moreover, the case with the smallest borehole diameter of 5 mm has a clear bi-wing fracture.

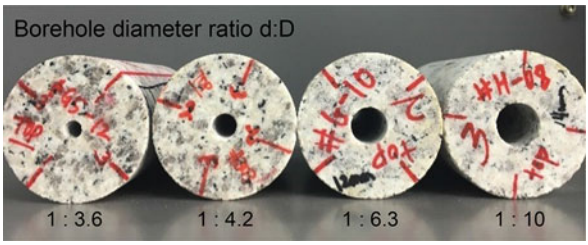

Fig. 4.8 Granite samples with different borehole diameters. (Zhuang et al. 2018c)

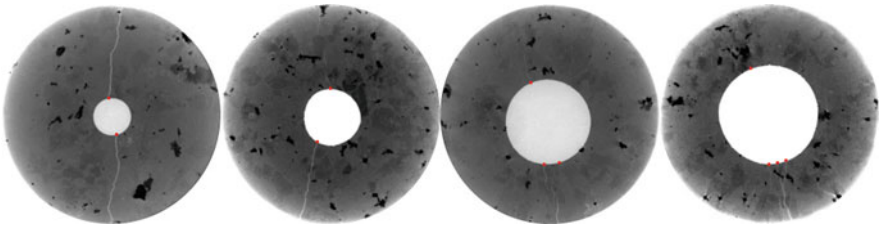

Fig. 4.9 Induced fractures in the four specimens under injection rate of 50 mm^3/s: (**a**) d = 5 mm, (**b**) d = 8 mm, (**c**) d = 12 mm, (**d**) d = 14 mm. (Zhuang et al. 2018c)

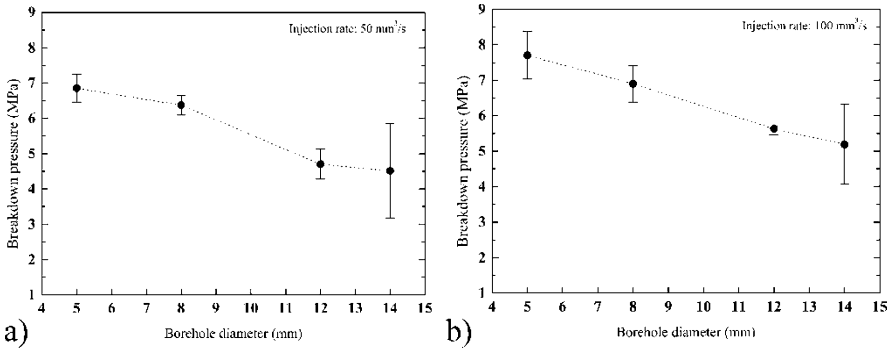

Fig. 4.10 Breakdown pressures at different borehole sizes: (**a**) Injection rate 50 mm^3/s and (**b**) Injection rate 100 mm^3/s. (Zhuang et al. 2018c)

Figure 4.10 compares the average BP and corresponding standard deviations for the four different borehole diameters under injection rates of 50 and 100 mm^3/s. In both cases, BP decreases with increasing borehole diameter. For a given borehole diameter, BP is higher at the higher injection rate.

The estimated pressurization rate, defined as the slope of the approximately linear section of the injection pressure–time curve before breakdown, is plotted in Fig. 4.11. For a given injection rate, the pressurization rate decreases with increasing borehole size. The magnitude is approximately doubled when the injection rate increases from 50 to 100 mm^3/s.

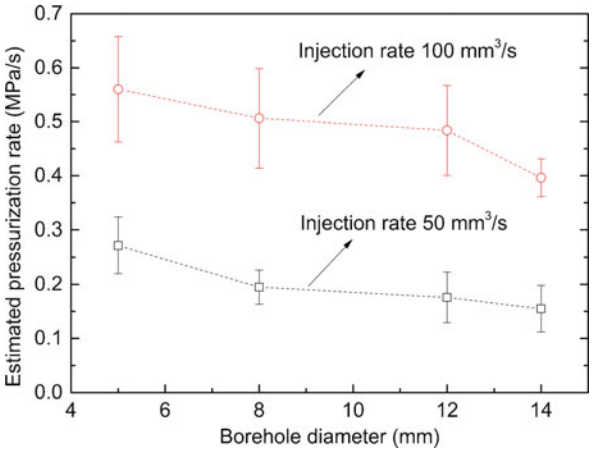

Fig. 4.11 Comparison of the estimated pressurization rate. (Zhuang et al. 2018c)

4.4.3 Influence of Injection Rate and Fluid Infiltration

Most laboratory hydraulic fracturing tests are performed under injection rate control, largely because fluid injection in the field is usually controlled by injection rate or injection volume. The injection rate and pressurization rate correlate to each other, although the relationship between them may not always be linear. In this section, injection rate influence is investigated with and without considering fluid infiltration. All the specimens have borehole diameter of 8 mm.

4.4.3.1 Injection Rate Effect Considering Fluid Infiltration

Figure 4.12 shows injection pressure with respect to total injected volume for H specimens under seven different injection rates from 1 to 100 mm^3/s. The volume is calculated as the injection rate (q) multiplied by injection time (t). The x-axis gives the total injected volume instead of injection time, because the range of the total injection time values is very large, making it difficult to view the result clearly on a linear time scale. Note that the total injected volume does not mean the volume of water infiltrating into the specimen, as some water was discharged through the outer surface of the cylindrical rock sample. The onset section of each curve shows a slow increase in injection pressure, because there was a small volume of air remaining in the booster, which delayed the water compression that provided pressure.

The figure shows two curve patterns. The first is for low injection rates (1–25 mm^3/s) and has injection pressure increasing slowly with increasing injected volume before converging to a certain value, called the maximum injection pressure P_{max}. A peak injection pressure was not observed, indicating a lack of hydrofracturing. The second pattern occurred at high injection rates (50–100 mm^3/s): injection pressure increased more quickly than in the low-injection-rate patterns and reached the breakdown pressure (P_b). After the peak, the zero confining pressure

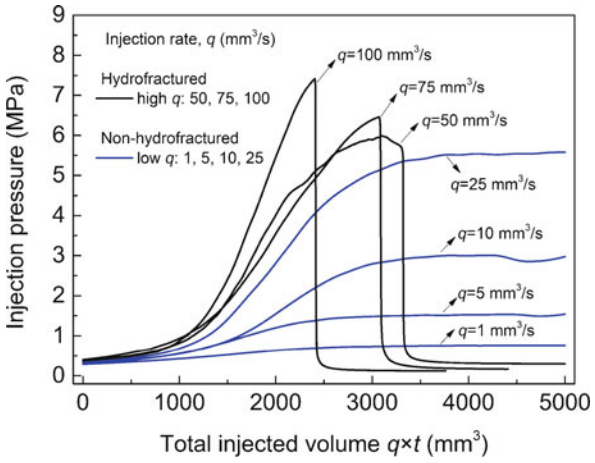

Fig. 4.12 Injection pressure plotted with respect to total pumped volume at different injection rates for H specimens at zero confining pressure. (Zhuang et al. 2019a)

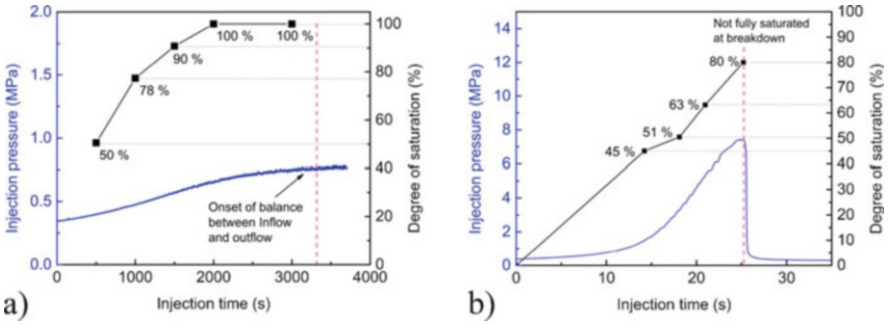

Fig. 4.13 Injection pressure and degree of saturation with respect to injection time: (**a**) Injection rate $q = 1$ mm^3/s and (**b**) $q = 100$ mm^3/s. (Zhuang et al. 2019a)

caused the injection pressure to drop very quickly to zero. For both types of curve, the ascending section was not linear, especially when approaching P_{max} or P_b.

Figure 4.13 compares the variations in injection pressure and degree of saturation at a low (1 mm^3/s) and a high (100 mm^3/s) injection rate. Zhuang et al. (2019a) reported details on the measurement of the degree of saturation. At the low injection rate, the specimen reached full saturation after 2000 s, while the injection pressure was only 0.45 MPa. At saturation, inflow and outflow reached equilibrium, and injection pressure could not increase any more. As a result, the specimen was not hydrofractured. At the high injection rate, the degree of saturation was less than 80% when the injection pressure was close to the BP, meaning that the specimen was fractured before it was fully saturated. Similar to the low injection rate, tests at injection rates of 10 and 25 mm^3/s had maximum injection pressures of only 2.06 and 5.06 MPa, respectively, as full saturation was approached. These values are much lower than the threshold BP (~6.0 MPa), and thus the specimens were not hydrofractured. At an injection rate of 50 mm^3/s, breakdown was achieved at a degree of saturation of ~80%.

Numerical simulation on the above experiemental results using UDEC shows that the diffusion length decreases with increasing pressurization rate, as a result breakdown pressure increases (Xie et al. 2018).

4.4.3.2 Injection Rate Effect Excluding the Influence of Fluid Infiltration: Sleeve Fracturing

In sleeve fracturing tests, the borehole and the top and bottom surfaces of the sample were sleeved with a latex cover to prevent water infiltration. Figure 4.14 compares the curves of injection pressure with respect to the total injected volume at injection rates of 1, 10, 50 and 100 mm^3/s for tests with and without sleeves. Breakdown was observed in the sleeve fracturing tests at both low and high injection rates. After the early stage, injection pressure increased almost linearly until breakdown, regardless of injection rate. Moreover, injection pressure developed much more quickly in the sleeve fracturing tests, because no water was lost during injection.

Figure 4.15 compares the BPs in sleeve fracturing and hydraulic fracturing tests at different injection rates. The sleeve fracturing BPs of H specimens are 18–23 MPa, more than double those in hydraulic fracturing. Established breakdown prediction models that mainly consider in situ stresses, tensile strength and the pore pressure effect are not able to predict the anomalously high BP. This phenomenon was also reported by Brenne et al. (2013), who used a fracture mechanics model to explain the high breakdown pressures in sleeve fracturing tests.

Figure 4.16 shows a typical example of injection pressure variation together with the amplitude of induced AE hits detected during the hydraulic fracturing of an H specimen at an injection rate of 100 mm^3/s and zero confining pressure. The induced AE starts at an injection pressure of ~7.0 MPa, which is close to the BTS of the specimen's rift plane. This indicates that cracks were generated near the borehole along the rift plane when the injection pressure exceeded the tensile strength.

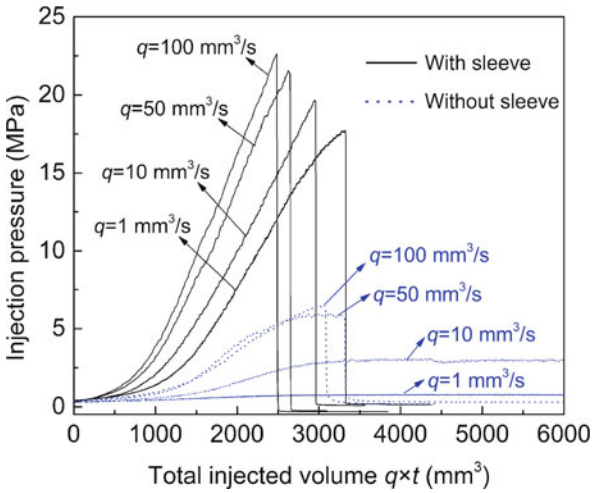

Fig. 4.14 Comparison of injection pressure variation between tests with and without sleeve in the borehole. (Zhuang et al. 2019a)

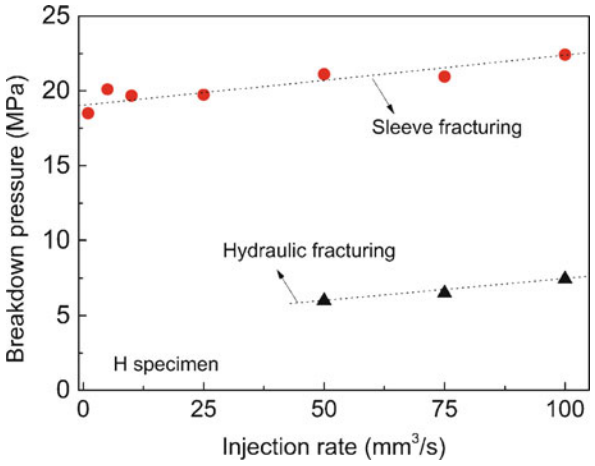

Fig. 4.15 Comparison of breakdown pressures between hydraulic fracturing and sleeve fracturing. (Zhuang et al. 2019a)

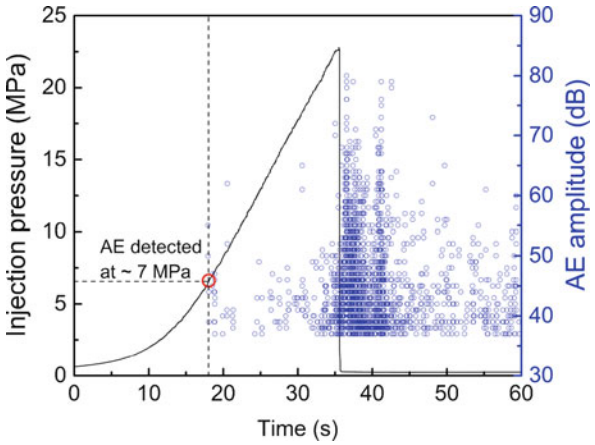

Fig. 4.16 Acoustic emission measurements in sleeve fracturing test at $q = 100$ mm^3/s. (Zhuang et al. 2019)

However, with a sleeve around the borehole, there was no water leakage into the specimen, and fluid pressure was not able to reach the inside of the initial cracks to promote fracture propagation. Injection pressure therefore continued to increase linearly because of the confined space of the borehole until the specimen was totally fractured or failed. The resulting breakdown pressure is influenced by the stress gradient in the sample, which depends on the specimen size.

4.4.4 Influence of Injection Fluid Viscosity on Hydraulic Fracturing

Figure 4.17 compares the breakdown pressures measured using tap water and oils injected at different rates. The water has a viscosity of ~1 cp at room temperature,

while the three tested types of oil have viscosities of 80, 122 and 152 cp and densities of 0.855, 0.858 and 0.861 g/cm^3 at 15 °C, respectively. Specimens were not fractured by water at low injection rates of 5 and 25 mm^3/s, as explained in the previous section. Except for the tests at the very low injection rate of 5 mm^3/s, BP increases with increasing viscosity.

The volume of infiltrated fluid was measured by weighing samples before and after injection. The results in Fig. 4.18 show that for a given injection rate, the total volume of infiltrated fluid increases with the decreasing viscosity of fluid. The result for the infiltration of oil (122 cp) was excluded as the data were unavailable.

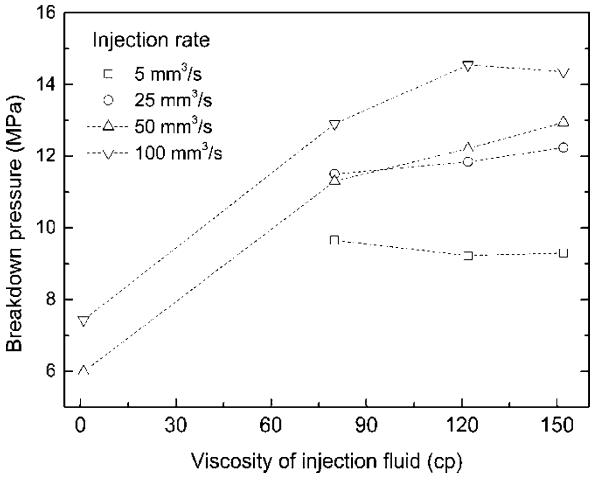

Fig. 4.17 Comparison of breakdown pressures using different viscosities of injection fluids

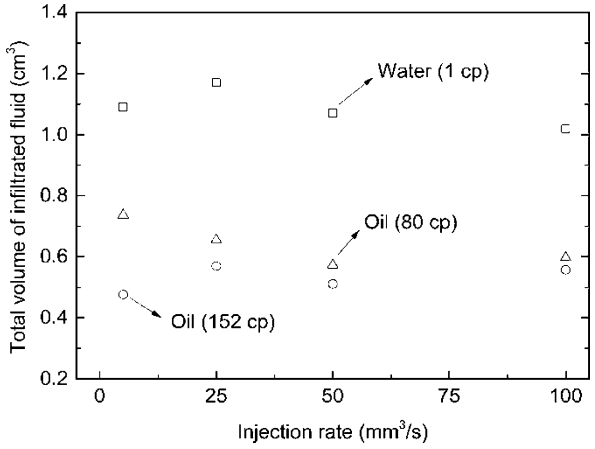

Fig. 4.18 Comparison of infiltrated fluid at different injection rates using water and oils

4.4.5 *Cyclic Hydraulic Fracturing*

Laboratory tests of G granite specimens (sample diameter, 50 mm; borehole diameter, 8 mm) were conducted by applying both continuous and cyclic injection schemes. Figure 4.19 compares typical injection pressures, injection rate–time curves and amplitudes of AE hits for both injection patterns.

The continuous injection used water at a constant injection rate of 50 mm^3/s until breakdown occurred at an injection pressure of 7.0 MPa. Nearly all AE events were detected immediately after the breakdown, and the maximum amplitude was 94 dB. Cyclic injection alternated between a high (50 mm^3/s) and zero injection rate, and the interval between them was controlled by the upper and lower bounds of injection pressures for each cycle, which were ~6.2 and ~1.0 MPa in this case. The sample finally failed after 116 injection cycles. The maximum AE amplitude was 72 dB, which was 22 dB lower than that during continuous injection. Injection pressure did not decrease to almost zero like in continuous injection, indicating that the fracture did not propagate to the outside boundary (Zhuang et al. 2019a). Water was still being injected, and the pressure reached a relatively stable value above 4 MPa, which was lower than the given upper bound pressure of 6.2 MPa. No shut-in was performed, and no other cycle was registered.

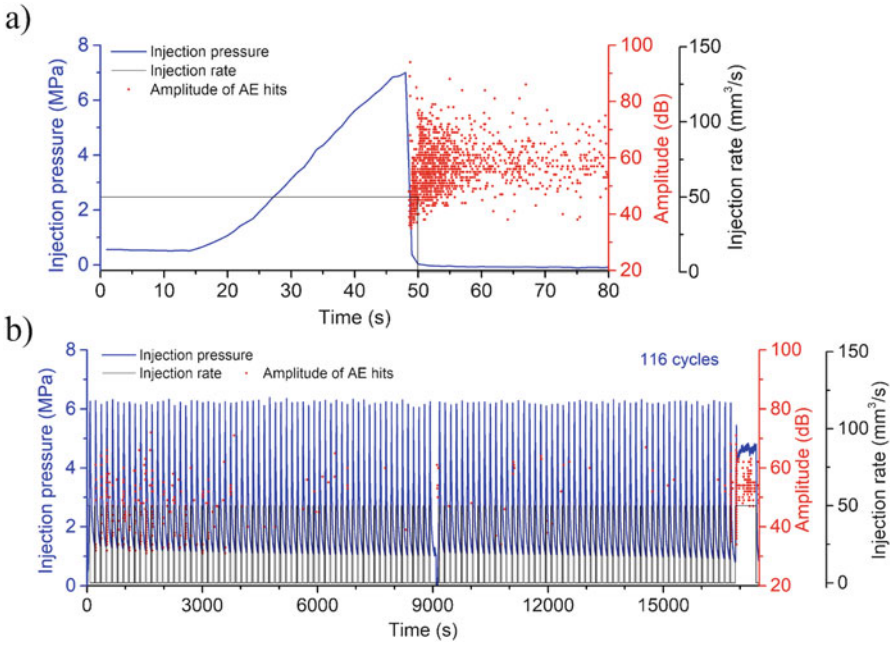

Fig. 4.19 Injection pressure-injection time curve for (**a**) monotonic injection and (**b**) cyclic injection of G specimens

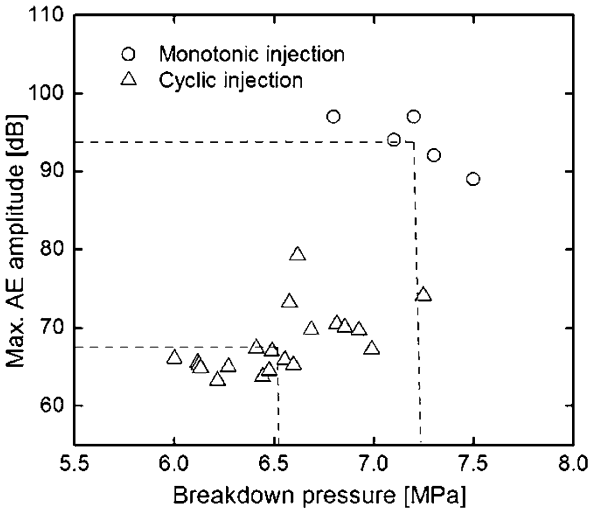

Fig. 4.20 Breakdown pressure and maximum amplitude of AE event during 5 continuous and 20 cyclic injection tests of granite core samples. Dashed lines indicate average values of monotonic and cyclic injection, respectively. (Zang et al. 2019)

Figure 4.20 shows the maximum amplitude with respect to breakdown pressure for tests conducted under continuous and cyclic injection. Five specimens were tested under continuous water injection (circles) at a rate of 50 mm^3/s, and the average breakdown pressure was 7.18 MPa. For the second set of tests, 20 specimens were tested under cyclic injection (triangles in Fig. 4.20). Each test had a maximum injection pressure (lower than the monotonic average) set as an upper limit, and cycling was repeated indefinitely until the specimen failed. These maximum pressures represent a range of 77% to 101% of the average BP measured from hydraulic fracturing tests with continuous injection. The average BP of the 20 cyclic cases was 6.52 MPa, although the specimens failed after different numbers of cycles. The average maximum amplitude of AEs was 93.8 dB for monotonic injection and 67.8 dB for cyclic injection. On average for Pocheon granite, a cyclic injection pattern reduces BP by ~10% and the average maximum magnitude of AE by 26 dB when the experimental setup and samples are otherwise identical.

4.5 Acoustic Emission Monitoring of the Initiation and Propagation of Hydraulic Fractures

AE monitoring is a non-destructive technique used to detect, record or examine acoustic waves generated by diverse sources due to stress changes in a material or structure. Therefore, it is a useful technique for monitoring the structures or crack initiation and propagation in a material subjected to a load. Figure 4.21 shows AE measurements for a cylindrical rock sample loaded vertically. Atomic-scale movements inside the sample generate acoustic waves that are recorded by an AE sensor

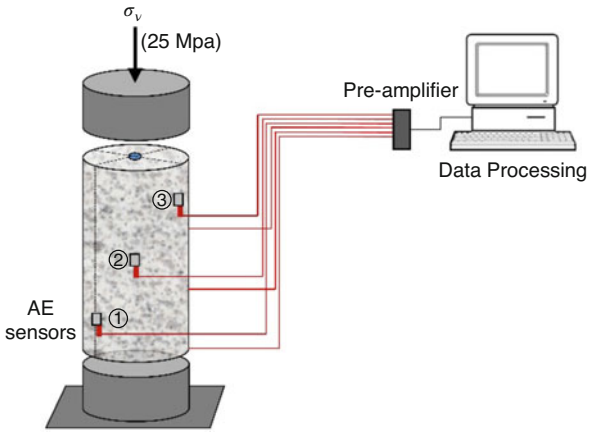

Fig. 4.21 Schematic diagram of AE monitoring during rock sample testing under axial load. (Diaz et al. 2018b)

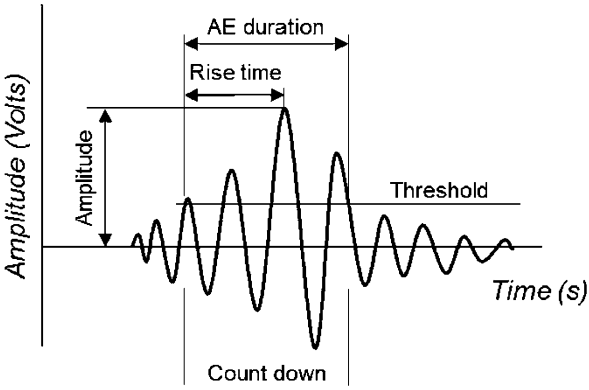

Fig. 4.22 Schematic of a typical AE waveform recorded during monitoring. (MISTRAS 2014)

directly connected to a pre-amplifier signal unit, which sends the data to a computer for storage and analysis.

4.5.1 Basic AE Signal Parameters

A waveform can cause AEs with various properties, although there are some basic parameters used for monitoring and analysis. Figure 4.22 illustrates a typical AE waveform recorded during material testing. The Amplitude represents the maximum positive or negative value during an AE hit; it is typically given in dB. Equation (4.4) describes the relation that defines the amplitude:

$$dB = 20\,log\left(\frac{V_{max}}{1\mu - volt}\right) - (Preamplifier\ Gain \in dB) \tag{4.4}$$

where V_{max} is the maximum amplitude measured in volt and divided by the reference voltage. The preamplifier gain (given in dB) is defined by the user based on the AE source type.

Values below a certain level are counted as noise and excluded from the analysis. This Threshold is a crucial parameter that controls the other parameters' values.

Another important parameter is the AE Duration, which is defined as the time between the first and last waveforms above the threshold.

Similarly, the Rise time is also affected by the threshold. It is defined as the time from the first waveform above the threshold to the peak amplitude.

Finally, the Counts is another value determined from the waveform and defined by the threshold. It refers to the number of AE waveforms that occur above the threshold value.

Other derived parameters such as the Average frequency, Energy and Absolute energy are also important. The average frequency is the ratio between the number of AE counts and the AE duration. The energy is calculated as the integral of the voltage signal over the AE hit duration. The absolute energy refers to the true energy of the hit, computed from the integral of the squared voltage signal divided by the reference resistance over the duration, and commonly given in joule.

4.5.2 AE Monitoring Setup

Figure 4.23 depicts the AE monitoring setup during the laboratory hydraulic fracturing tests of granite cores under zero confining pressure (Diaz et al. 2018b). The granite cores are G specimens of the type shown in Fig. 4.5, having a borehole diameter of 5 mm. After the sample is set on the pedestal, an upper cylindrical cap is placed on its top, and the plastic membrane is adjusted. The upper part of the equipment is then carefully placed and rested on four bars with stops. The sample is next loaded to a predefined level before AE sensors are attached to its surface with a coupling agent to facilitate contact between the material and the sensor surface. Confining pressure is not applied. This arrangement allows for AE sensors to be installed directly on the sample (with membrane) to enable the location of AE events during testing.

The AE monitoring system (Physical Acoustic Corporation, MISTRAS Group, USA) includes an array of six Nano30 sensors with a frequency domain of 125–750 kHz placed at different heights, as illustrated in Fig. 4.23. The location of each sensor is later represented in the acquisition software to enable event location during post-processing. A pre-amplifier gain value of 40 dB is selected for all the tests.

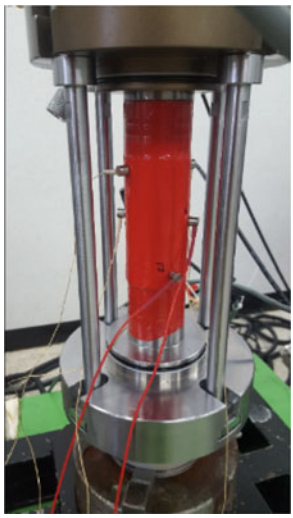

Fig. 4.23 Installation of AE sensors on a cylindrical sample

4.5.3 AE Raw Data Filtering

During AE monitoring, many signals are recorded, including noise that should be discarded. Sagar and Prasad (2011) state that low-magnitude signals should be counted as background noise if their duration is less than 10 μs and count less than two. Signals with a duration longer than a pre-defined frame time should also be removed. MISTRAS Group (2014) suggested to use the following equation to define the appropriate hit definition time (HDT):

$$HDT = 1024x\left(\frac{L}{S}\right) - P, \tag{4.5}$$

where L is the signal length in μs, S is the sample rate in millions of samples per second, and P is the pre-trigger time in μs.

Another parameter that can be used to discriminate signals is the Energy: signals with an energy equal to zero are advised to be removed (Nguye-Tat et al. 2017).

4.5.4 Analysis Results

The following AE monitoring results were obtained for similar specimens tested under continuous and cyclic injection (as described in Sect. 4.4.5). Figure 4.24 shows the injection pressure, accumulated hits and hit rate with respect to injection time for continuous and cyclic injection. During continuous injection, AE activity was detected immediately before breakdown, at which point the accumulated number of AE hits rapidly increased. Similarly, the hit rate shows a small increment

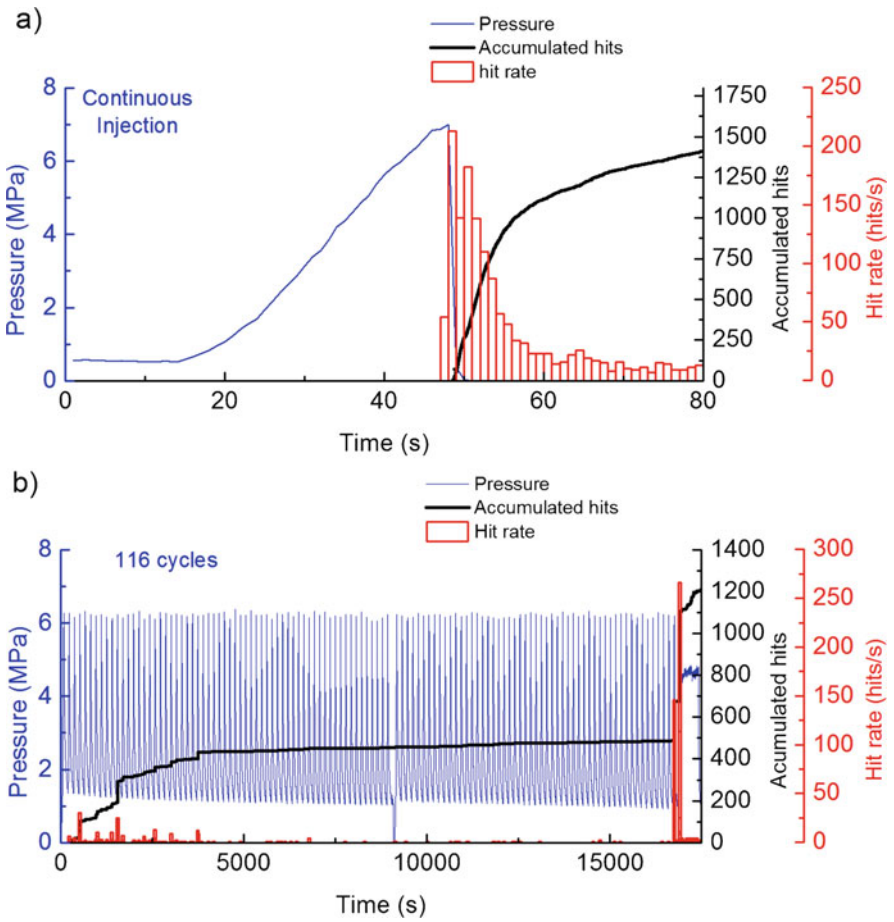

Fig. 4.24 Injection pressure, accumulated AE hits and AE hit rate for (**a**) continuous and (**b**) cyclic injection of the G specimens

before breakdown followed by the peak value right at the moment of failure. Relatively high hit rates continue for a few seconds as the fracture reaches its final size before the hit rate decreases considerably. On the other hand, the specimen tested under cyclic injection failed after 116 cycles. The accumulated number of hits register early AE activity during the first 4000 s. The extended period of injection, compared with continuous injection, could allow the dilation of pre-existing microcracks in the granite that cause the early AE. The early activity is followed by a period of relatively stable behaviour with minimal AE activity. Close to breakdown, there are two jumps in the accumulated number of hits: one at the last complete cycle and another during the pressure increase of the next cycle that did not reach a pressure above 5 MPa. This implies that the failure occurred in two stages: one small opening during the last complete cycle, followed by the major fracture opening as indicated by the maximum hit rate of 266 hits/s.

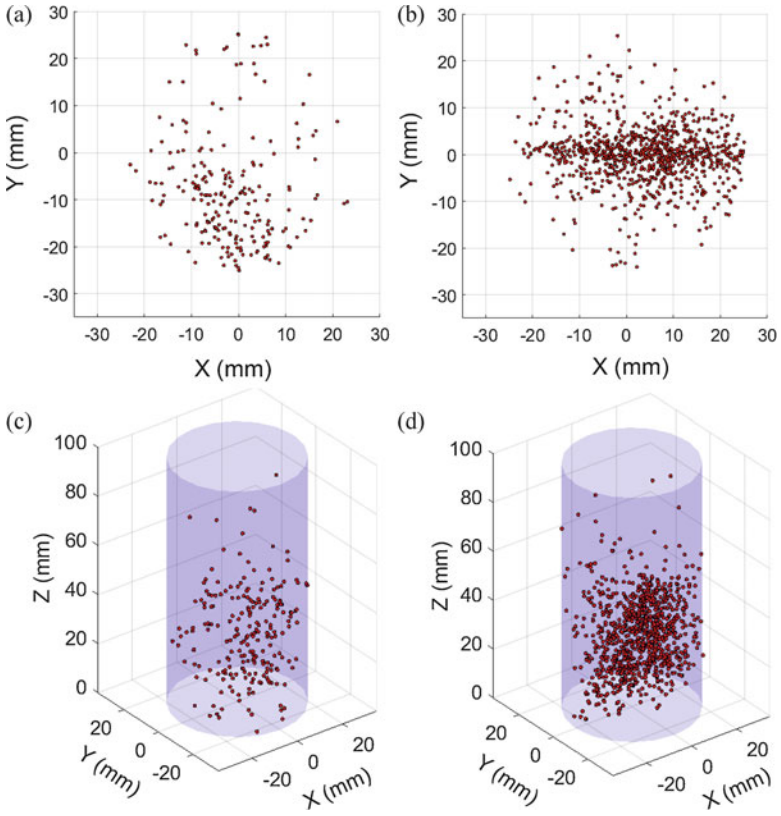

Fig. 4.25 Location of AE events in 2D and 3D for (**a**) continuous and (**b**) cyclic injection of the G specimens

Figure 4.25 shows the locations of the AE events for continuous and cyclic injection. Fewer events are plotted for continuous injection, and the AE cloud does not correlate with the fracture size or location. In contrast, the AE events for cyclic injection show a clear orientation along the x-axis (which represents the direction of the rift plane) and most of the AE cloud is located in the lower half of the sample.

4.6 X-Ray CT Observation and Characterization of Hydraulic Fractures

The characterization of length, aperture, roughness and orientation of hydraulic fractures is important, because these properties determine whether hydraulic stimulation has improved reservoir performance. X-ray CT is used here to capture hydraulic fractures, focusing on the initiation and propagation of the fractures during cyclic injection.

4.6.1 X-Ray CT Equipment

The X-ray CT scanning system (the PCT X-EYE system at the Korea Institute of Civil Engineering and Building Technology, KICT) consists of three different X-ray source tubes with different energy levels (120, 225, and 320 kV) and a flat panel detector of 1024 × 1024 pixels. The 225 kV source tube for X-ray generation was used to fulfil the optimal scanning condition for the present study, considering the density and size of the specimens. Each specimen was irradiated with X-rays over its circumference by rotating it 360° in 1800 equally spaced increments.

Conventionally, artifacts can arise in the reconstructed volume of CT images (Cnudde and Boone 2013). They are caused mainly by the different lengths of the X-ray paths when scanning irregularly shaped materials, and therefore can be largely avoided by using cylindrical specimens. However, ring artefacts can be still found in the images, because they are caused by miscalibration or failure of one or more detector elements in the CT scanner. They occur close to the isocentre of the scan and are usually visible on multiple slices at the same location. This is a common problem in cranial CT and is encountered in this study. Ring artifacts are removed using fast Fourier transform filtering.

4.6.2 Comparison of Hydraulic Fracture Patterns

Figure 4.26 compares representative CT image sections for G specimens fractured in three different cases: monotonic, 473 cycles, and 839 cycles of injection. Zang et al. (2019) reported full details of the test conditions. Quantitative analysis of the fracture paths was possible through extracting patterns from the CT images (Fig. 4.26b), which revealed that monotonic injection led to larger apertures than cyclic fracturing. The complexity of fracture patterns was assessed by computing the tortuosity (length of fracture path divided by the shortest distance between fracture tips), whose values are 1.04, 1.05, and 1.09 for the three cases displayed in Fig. 4.26b, from left to right, although a limited domain is considered for this measurement.

4.6.3 Evolution of Hydraulic Fractures during Cyclic Injection

The evolution of fracturing during cyclic hydraulic injection is monitored here via the first attempt at combining hydraulic fracturing tests (G specimens of Pocheon granite, 30 mm diameter) and CT scanning. The tests were performed outside of the X-ray chamber.

Water was injected at a rate of 50 mm^3/s up to the point when the injection pressure reached a threshold value of 4 MPa. This value was set by referring to the

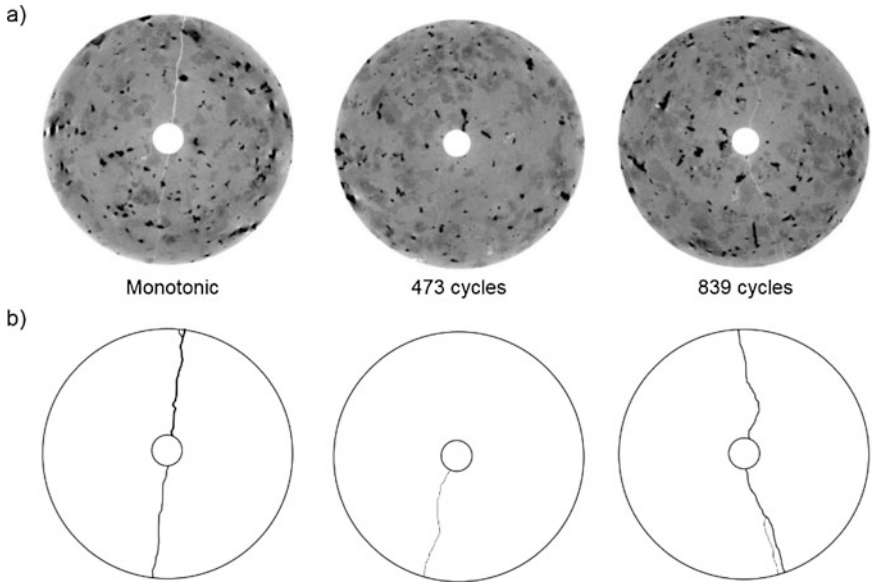

Fig. 4.26 Visualized fracture pattern of granite cores after monotonic and cyclic injection. (**a**) X-ray CT images and (**b**) fracture images. (Zang et al. 2019)

breakdown pressure (~6 MPa) during continuous injection at the same injection rate and stress conditions (Zhuang et al. 2018d). Injection was frequently stopped and resumed after the injection pressure was reduced to ~1 MPa to start a new cycle. During testing, the sample was repeatedly CT scanned after the completion of a number of injection cycles (i.e., it was in a stress-free state). The sample finally failed after 29 cycles of injection. Figure 4.27 shows CT images taken at the beginning and after 20, 25, 28 and 29 injection cycles. The images compare the same location, at a height of 1.4 mm from the bottom.

Figure 4.27a shows the initial state of the sample before injection; one short pre-existing crack was located near the surface. After 20 cycles (Fig. 4.27b), fractures of different lengths had initiated at both sides of the borehole cutting across quartz and feldspar grains. After five more cycles (Fig. 4.27c), the upper fracture had extended farther, whereas the lower fracture remained unchanged. Later, after three further cycles (Fig. 4.27d), the upper fracture was almost unchanged, while the lower fracture extended to reach the boundary of the feldspar grain. Finally, in Fig. 4.27e, the upper fracture extended along two mica grains, and the lower fracture extended farther along feldspar grain boundaries to the outer surface.

The above fracture evolution is limited to the specific examined height of the sample, and different patterns will emerge at different locations. Nevertheless, the evolution indicates that cyclic injection with an injection pressure lower than the monotonic breakdown pressure can propagate fractures, and in particular generate fractures along feldspar–quartz or mica–quartz grain boundaries, which are less strongly bonded than the grains themselves (Zhuang et al. 2018a).

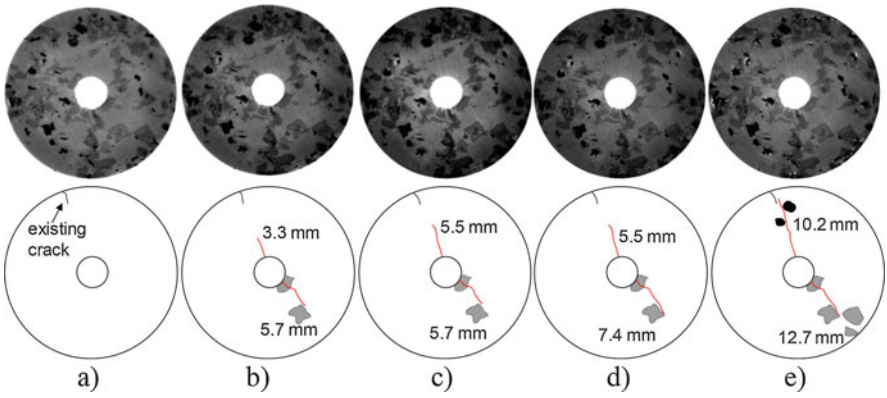

Fig. 4.27 X-ray CT images and corresponding sketches showing fracture development under cyclic injection. (**a**) initial state, (**b**) 20 cycles, (**c**) 25 cycles, (**d**) 28 cycles, and (**e**) 29 cycles. For the sketches, Red line: hydraulic fracture, grey: feldspar grain, black: mica grain. Values represent the total length of fracture at each side of the borehole

4.7 Discussion

The prediction of fracture initiation and propagation in rocks is difficult, particularly for samples with pre-existing cracks. AE monitoring can help elucidate fracture initiation and propagation, but is influenced by many factors, particularly the installation of AE sensors and data filtering. Most BP models work only for specific conditions, as BP is not an inherent characteristic of rock, but depends on various factors including those discussed in this study. This study's experimental findings on the influence of injection rate, borehole size and viscosity of injection fluid are consistent with past studies on the hydraulic fracturing of granites (Haimson and Zhao 1991; Chen et al. 2015).

We noted large differences in the BPs of granite cores fractured hydraulically and using a sleeve, varying with borehole size (Zhuang et al. 2018d) and rock type (Brenne et al. 2013). The linear elastic fracture mechanics model, assuming the pre-existence of a symmetrical double crack with half-length a (Rummel 1987; Haimson and Zhao 1991), is used to interpret the differences. The Pocheon granite used here has a measured tensile toughness K_{Ic} of 0.963 MPa·$m^{0.5}$ for the rift plane, where fractures were mainly generated. Figure 4.28 compares experimental measurements with theoretical predictions of BP assuming a crack length a = 3.0 mm. Haimson and Zhao (1991) assumed a = 4.3 mm for a different Lac du Bonnet granite to that of the present study.

The experimental and theoretical values show similar trends for BP with increasing borehole diameter, despite discrepancies of ~1 MPa for HF tests on large borehole diameters of 12 and 14 mm, and ~2 MPa for all of the sleeve fracturing tests. The fracturing mechanics model performs relatively well in explaining the experimental results.

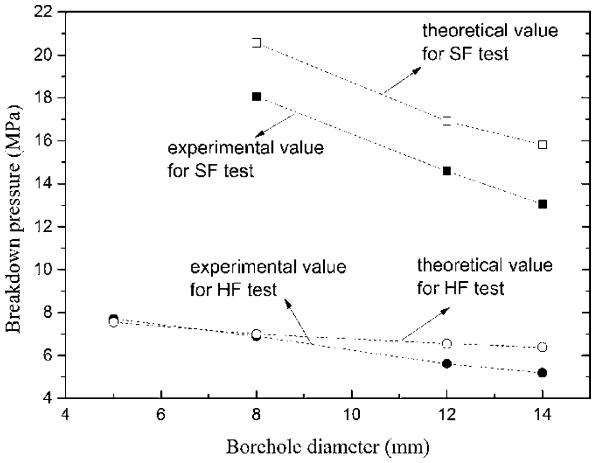

Fig. 4.28 Comparison of BP between theoretical and experimental values. *HF* hydraulic fracturing, *SF* sleeve fracturing. (Zhuang et al. 2018c)

However, the ideal case of two symmetric pre-existing cracks with the same length near the borehole is rare in the laboratory and practically non-existent in the field. CT observations also show that most hydraulic fractures generated in granite core samples are not symmetric along the borehole axes and that the propagation is not simultaneous even if bi-wing fractures were generated on both sides of borehole.

The initiation and propagation of fractures could become more complex when samples become large enough to have significant scale effects. An experimental study on granite blocks by Zhao et al. (1996) showed that the fracture initiation pressure is equal to the breakdown pressure under isotropic far-field horizontal stresses, while for unequal far-field horizontal stresses the fracture initiation occurs considerably before breakdown. The injection fluid (i.e., gas) and rock texture (particularly grain size and pre-existing microcracks) significantly affect the fracturing mechanism of granite (Ishida et al. 2000; Chen et al. 2015). The influence of existing natural fractures was not considered in either above study or this study.

The experimental results of this study are limited to uniaxial and biaxial stress conditions, while in situ stresses are usually different for the three principal directions. Further experimental studies on the hydraulic fracturing behaviour of the same Pocheon granite under a true triaxial stress state have been reported by Zhuang et al. (2018a, b) and Diaz et al. (2018a, c).

4.8 Summary

This chapter covers a series of laboratory experimental studies on the hydraulic fracturing of granite cores under uniaxial and biaxial stress conditions. The effects of injection rate, fluid infiltration, fluid viscosity, borehole size and injection scheme are analysed. AE monitoring and X-ray CT technology aided the interpretation of the

results and shed light on the processes of fracture initiation and propagation. Some key points are summarized as follows.

1. Injection pressure increased with increasing injection rate, although two types of increment pattern were observed. In the hydraulic fracturing tests with fluid infiltration, low injection rates produced slowly increasing pressure curves that reached a certain value with no peak pressure. Conversely, higher injection rates resulted in rapidly increasing pressure curves that led to breakdown with clear peak pressures.
2. During sleeve fracturing tests that excluded fluid infiltration into the rock specimen, breakdown occurred even at low injection rates, and BP was double that observed during hydraulic fracturing at the same injection rate.
3. Breakdown pressure (BP) increased almost linearly with increasing confining pressure, although the rate of increment was affected by the injection rate. BP increased with increasing viscosity of the injection fluid, and it decreased with increasing borehole diameter.
4. Hydraulic fracturing by cyclic injection reduced both the BP and the maximum amplitude of AE compared with those during continuous injection.
5. Finally, CT scanning enabled observation of the fracturing process at the mineral scale for granite cores and characterization of fracture patterns and complexity (i.e., tortuosity).

References

Brenne S, Molenda M, Stöckhert F, Alber M (2013) Hydraulic and sleeve fracturing laboratory experiments on 6 rock types. In: Jeffrey R (ed) Effective and sustainable hydraulic fracturing. IntechOpen, London, pp 425–436

Chen Y, Nagaya Y, Ishida T (2015) Observations of fractures induced by hydraulic fracturing in anisotropic granite. Rock Mech Rock Eng 48:1455–1461

Cnudde V, Boone MN (2013) High-resolution X-ray computed tomography in geosciences: a review of the current technology and applications. Earth-Sci Rev 123:1–17

Detournay E, Cheng A (1992) Influence of pressurization rate on the magnitude of the breakdown pressure. In: Tillerson JR, Wawersik WR (eds) Rock mechanics. Balkema, Rotterdam, pp 325–333

Diaz MB, Jung SG, Zhuang L, Kim KY (2018a) Comparison of acoustic emission activity in conventional and cyclic hydraulic fracturing in cubic granite samples under tri-axial stress state. In: Proceedings of the 52nd US rock mechanics/geomechanics symposium. ARMA, Seattle, pp 18–1160

Diaz MB, Jung SG, Zhuang L, Kim KY, Zimmermann G, Hofmann H, Zang A, Stephansson O, Min KB (2018b) Hydraulic, mechanical and seismic observations during hydraulic fracturing by cyclic injection on Pocheon granite. In: Proceedings of the 10th Asian rock mechanics symposium, Singapore

Diaz M, Jung SG, Zhuang L, Kim KY, Hofmann H, Min KB, Zang A, Zimmermann G, Stephansson O, Yoon JS (2018c) Laboratory investigation of hydraulic fracturing of granite under true triaxial stress state using different injection schemes – Part 2. Induced seismicity. In: Proceedings of international conference on coupled processes in fractured geological media: observation, modeling, and application, Nov 12–14, Wuhan

Gischig V, Preisig G (2015) Hydro-fracturing versus hydro-shearing: a critical assessment of two distinct reservoir stimulation mechanisms. In: Proceedings of the 13th international congress of rock mechanics, ISRM 2015, Montréal, Canada

Guo F, Morgenstern NR, Scott J (1993) Interpretation of hydraulic fracturing breakdown pressure. Int J Rock Mech Min Sci Geomech Abstr 30(6):617–626

Haimson BC (1999) Six hydraulic fracturing campaigns at the URL, Manitoba. In: Proceedings of 9th ISRM congress, 25–28 August, Paris

Haimson B, Doe TW (1983) State of stress, permeability, and fractures in the Precambrian granite of Northern Illinois. J Geophys Res 88(B9):7355–7372

Haimson B, Fairhurst C (1967) Initiation and extension of hydraulic fractures in rocks. Soc Pet Eng J 7(03):310–318

Haimson B (1975) The state of stress in the earth's crust. Rev Geophys Space Phys 13(3):350–352

Haimson BC, Lee CF (1980) Hydrofracturing stress determination at Darlington, Ontario. In: Proceedings of 13th Canadian symposium on rock mechanics, Canadian Institute of Mining and Metallurgy, pp 42–50

Haimson BC, Zhao Z (1991) Effect of borehole size and pressurization rate on hydraulic fracturing breakdown pressure. In: Roegiers JC (ed) Rock mechanics as a multidisciplinary science. Balkema, Rotterdam, pp 191–199

Hofmann H, Zimmermann G, Zang A, Yoon JS, Stephansson O, Kim KY, Zhuang L, Diaz M, Min KB (2018a) Comparison of cyclic and constant fluid injection in granitic rock at different scales. In: Proceedings of the 52nd US rock mechanics/geomechanics symposium. ARMA, Seattle, pp 18–691

Hofmann H, Zimmermann G, Zang A, Min KB (2018b) Cyclic soft stimulation (CSS): a new fluid injection protocol and traffic light system to mitigate seismic risks of hydraulic stimulation treatments. Geotherm Energy 6:27

Hubbert KM, Willis DG (1957) Mechanics of hydraulic fracturing. Petrol Trans AIME 210:153–168

Ishida T, Chen Q, Mizuta Y (1997) Effect of injected water on hydraulic fracturing deduced from acoustic emission monitoring. Pure Appl Geophys 150:627–646

Ishida T, Sasaki S, Matsunaga I, Chen Q, Mizuta Y (2000) Effect of grain size in granitic rocks on hydraulic fracturing mechanism. In: Proceedings of sessions of Geo-Denver 2000, trends in rock mechanics, geotechnical special publication no.102, ASCE, pp 128–139

Ishida T, Chen Q, Mizuta Y, Roegiers JC (2004) Influence of fluid viscosity on the hydraulic fracturing mechanism. J Energy Resour Technol 126:190–200

Ishida T, Aoyagi K, Niwa T, Chen Y, Murata S, Chen Q, Nakayama Y (2012) Acoustic emission monitoring of hydraulic fracturing laboratory experiment with supercritical and liquid CO_2. Geophys Res Lett 39(16), L16309:1–6

Morita N, Black AD, Fuh GF (1996) Borehole breakdown pressure with drilling fluids–I. Empirical results. Int J Rock Mech Min Sci Geomech Abstracts 33(1):39–51

MISTRAS Group Inc. (2014) Express-8 AE system user's manual

Nguyen-tat T, Ranaivomanana N, Balayssac JP (2017) Identification of shear-induced damage in concrete beams by Acoustic Emission. In: Proceedings of the 2nd International RILEM/COST conference on early age cracking and serviceability in cement-based materials and structures – EAC2, Brussels, Belgium

Rummel F (1987) Fracture mechanics approach to hydraulic fracturing stress measurements. In: Atkinson BK (ed) Fracture mechanics of rocks. Academic Press, London, pp 217–239

Sagar RV, Prasad BR (2011) An experimental study on acoustic emission energy as a quantitative measure of size independent specific fracture energy of concrete beams. Constr Build Mater 25 (5):2349–2357

Solberg P, Lockner D, Byerlee JD (1980) Hydraulic fracturing in granite under geothermal conditions. Int J Rock Mech Min Sci Geomech Abstr 17(1):25–33

Stephansson O, Semikova H, Zimmermann G, Zang A (2019) Laboratory pulse test of hydraulic fracturing on granitic sample cores from Äspö HRL, Sweden. Rock Mech Rock Eng 52:629–633

Xie L, Zhuang L, Kim KY, Min KB (2018) Simulating hydraulic fracturing in low permeable rock with consideration of fluid infiltration into rock matrix. In: The 10th Asian rock mechanics symposium, Oct 29–Nov 3, Singapore

Zang A, Yoon JS, Stephansson O, Heidbach O (2013) Fatigue hydraulic fracturing by cyclic reservoir treatment enhances permeability and reduces induced seismicity. Geophys J Int 195:1282–1287

Zang A, Stephansson O, Stenberg L, Plenkers K, Specht S, Milkereit C, Schill E, Kwiatek G, Dresen G, Zimmermann G, Dahm T, Weber M (2017) Hydraulic fracture monitoring in hard rock at 410 m depth with an advanced fluid-injection protocol and extensive sensor array. Geophys J Intl 208:790–813

Zang A, Zimmermann G, Hofmann H, Stephansson O, Min KB, Kim KY (2019) How to reduce fluid-injection-induced seismicity. Rock Mech Rock Eng 52:475–493

Zhao Z, Kim H, Haimson B (1996) Hydraulic fracturing initiation in granite. In: Aubertin, Hassani, Mitri (eds) Rock mechanics. Balkema, Rotterdam, pp 1279–1284

Zhuang L, Diaz MB, Jung SG, Kim KY (2016a) Cleavage dependent indirect tensile strength of Pocheon granite based on experiments and DEM simulation. Tunn Undergr Space 26:316–326

Zhuang L, Kim KY, Jung SG, Diaz M, Min KB, Park S, Zang A, Stephansson O, Zimmermann G, Yoon JS (2016b) Laboratory study on cyclic hydraulic fracturing of Pocheon granite in Korea. In: Proceedings of the 50th US rock mechanics/geomechanics symposium. ARMA, Houston, pp 16–163

Zhuang L, Kim KY, Jung SG, Nam YJ, Min KB, Park S, Zang A, Stephansson O, Zimmermann G, Yoon JS (2017) Laboratory evaluation of induced seismicity reduction and permeability enhancement effects of cyclic hydraulic fracturing. In: Proceedings of the 51st US rock mechanics/geomechanics symposium. ARMA, San Francisco, pp 17–757

Zhuang L, Kim KY, Jung SG, Diaz M, Min KB, Park S, Zang A, Stephansson O, Zimmermann G, Yoon JS (2018a) Cyclic hydraulic fracturing of cubic granite samples under triaxial stress state with acoustic emission, injectivity and fracture measurements. In: Proceedings of the 52nd US rock mechanics/geomechanics symposium. ARMA, Seattle, pp 18–297

Zhuang L, Kim KY, Jung SG, Diaz M, Hofmann H, Min KB, Zang A, Zimmermann G, Stephansson O, Yoon JS (2018b) Laboratory investigation of hydraulic fracturing of granite under true triaxial stress state using different injection schemes – Part 1. Permeability enhancement. In: Proceedings of international conference on coupled processes in fractured geological media: observation, modeling, and application, Nov 12–14, Wuhan

Zhuang L, Kim KY, Shin HS, Jung SG, Diaz M (2018c) Experimental investigation of effects of borehole size and pressurization rate on hydraulic fracturing breakdown pressure of granite. In: Proceedings the 10th Asian rock mechanics symposium, Oct 29–Nov 3, Singapore

Zhuang L, Kim KY, Yeom S, Jung SG, Diaz M (2018d) Preliminary laboratory study on initiation and propagation of hydraulic fractures in granite using X-ray Computed Tomography. In: Proceedings of international conference on geomechanics, geo-energy and geo-resources (IC3G2018), Sep 22–24, Chengdu

Zhuang L, Kim KY, Jung SG, Diaz M, Min KB (2019a) Effect of water infiltration, injection rate and anisotropy on hydraulic fracturing behavior of granite. Rock Mech Rock Eng 52:575–589

Zhuang L, Kim KY, Jung SG, Diaz M, Min KB, Zang A, Stephansson O, Zimmermann G, Yoon JS, Hofmann H (2019b) Cyclic hydraulic fracturing of Pocheon granite cores and its impact on breakdown pressure, acoustic emission amplitudes and injectivity. Int J Rock Mech Min Sci 122:104065

Zimmermann G, Zang A, Stephansson O, Klee G, Semiková H (2019) Permeability enhancement and fracture development of hydraulic in situ experiments in the Äspö Hard Rock Laboratory, Sweden. Rock Mech Rock Eng 52:495–515